Development of InSAR neutral atmospheric delay correction model by use of GNSS ZTD and its horizontal gradient

Yohei Kinoshita

***Abstract*—Interferometric Synthetic Aperture Radar (InSAR) often suffers from atmospheric disturbances due to the microwave propagation delay effect, which limits the surface displacement detection accuracy to an order of centimeters or more. Here I developed a new neutral atmospheric delay correction model for InSAR by using the global navigation satellite system (GNSS) zenith total delay (ZTD) and its horizontal gradient data. The proposed model at first retrieves the regularly gridded ZTD distribution at sea level and the linear height dependence from GNSS ZTD and gradient observations by the least squares method. Then, the gridded ZTD is projected onto the InSAR coordinate to correct the neutral atmospheric delay. I evaluated the correction model performance by applying it to L-band ALOS-2/PALSAR-2 ScanSAR interferograms over the Kanto plain in Japan. The correction result showed that by applying the proposed delay correction the phase standard deviation decreased by 33.87 % on average. By comparing it with the generic atmospheric correction online service for InSAR (GACOS) model and the correction by the Japanese regional mesoscale weather model (MSM), the proposed GNSS-based model outperformed others in my test case. The sensitivity test indicated that including the delay gradient could improve delay reproducibility under situations with fewer available GNSS stations. Although the proposed correction model's applicability depends on the number of available GNSS stations at the area of interest, the proposed model has a potential to effectively mitigate the neutral atmospheric delay and to improve the detection ability for small-amplitude surface displacements.**

***Index Terms*—Interferometric synthetic aperture radar (InSAR), atmospheric propagation delay, global navigation satellite system (GNSS), zenith total delay (ZTD), delay gradient.**

I. Introduction

THE interferometric synthetic aperture radar (InSAR) is now regarded as a powerful space geodetic technique to measure surface deformation as well as the global navigation satellite system (GNSS), but still suffers from the disturbance from the Earth's atmosphere. Such an effect in the space geodetic technique using the microwave is referred to as the atmospheric propagation delay effect, which limits the displacement detection ability of InSAR to an order of a few centimeters or larger [1]. The atmospheric delay effect can be divided into two components referred to as the effect due to the ionospheric disturbance (hereafter I called this as the ionospheric delay in accord with the custom, although the microwave phase is not delayed, but actually advanced in the ionosphere) and the delay effect in the neutral atmosphere. Recent progress succeeded in developing a robust correction method for the ionospheric phase variation in InSAR. The range split spectrum method (SSM) [2], which utilizes the SAR frequency modulation nature, has shown the usefulness to correct the InSAR ionospheric delay for both higher and lower frequency SAR systems (e.g. [3]–[5]). The neutral atmospheric delay is one of the remaining primary noise component in InSAR since it relates to the amount of the integrated water vapor along the microwave path and the atmospheric water vapor (most part of it exists in the lower troposphere) can fluctuate significantly in both space and time. In the extreme case, Kinoshita et al. [6] and Kinoshita and Furuya [7] showed that the amount of the neutral atmospheric delay in InSAR can reach over 20 cm in the line-of-sight (LOS) change when the well-developed cumulonimbus exists. To accomplish the millimeter-accuracy of the InSAR surface displacement measurement, a sophisticated atmospheric delay model should be required and need to be developed.

Many of previous studies tackled with the mitigation of the InSAR neutral atmospheric delay effect. In the early era of the InSAR research (from 1990s to 2000s), Sandwell and Sichoix [8] proposed the stacking approach, which performs an averaging manipulation to a stack of interferograms in the same observation geometry to mitigate the atmospheric delay signal in InSAR. The stacking approach assumes that the spatial distribution of atmospheric delay signal has no correlation when subsequent SAR observations span more than days. Although the stacking approach works well in cases using satellite SAR data because satellite recurrence intervals usually exceed several days (e.g. 12 days for Sentinel-1, 14 days for ALOS-2), this approach is not effective for the elevation-dependent (often called the stratified) delay signal because the stratified delay could have correlation for longer span (sometimes more than years). The time series approach, such as the Persistent Scatter Interferometry (PS-InSAR) [9] and the Small Baseline Subset (SBAS) [10], also has the similar characteristics to the stacking approach. Fujiwara et al. [11] focused on the approximately linear relationship between the stratified delay signal and the topographic height and proposed a simple empirical correction model using the digital elevation model (DEM). Since this model only uses topographic information and the InSAR phase itself to estimate

Y. Kinoshita was with the Department of Policy and Planning Sciences, Faculty of Engineering, Information and Systems, University of Tsukuba, Tsukuba, Ibaraki, Japan e-mail: ykinoshita@risk.tsukuba.ac.jp.

Manuscript received XXXX XX, 2021; revised XXXX XX, 202X.

the linear regression coefficients, the computational cost is very low and it is easy for users to implement it to their own InSAR processor. The disadvantages of the DEM-based model are that this model may overestimate the delay amount even if there are true displacement signals that also correlate with the topography (e.g. volcanic magma source inflation/deflation). Other approaches used external data to model the InSAR atmospheric propagation delay signal. For example, Doin et al. [12] used three kind of numerical weather model outputs such as ERA40 reanalysis and the operational analysis from the European Centre for Medium-Range Weather Forecasts (ECMWF), and the North American Regional Reanalysis to correct ERS and Envisat/ASAR interferograms and found that global numerical weather models can effectively correct the stratified delay component. Foster et al. [13] performed a non-hydrostatic meso-scale weather simulation with 1 km horizontal grid spacing by use of the MM5 model. Kinoshita et al. [6] compared the delay correction effectiveness of the Weather and Research Forecast (WRF) model, the non-hydrostatic numerical weather model with the classical DEM-based approach and the Meso-Scale Model objective analysis data provided every three hours by the Japan Meteorological Agency (JMA). Onn and Zebker [14] used the GNSS zenith total delay (ZTD) and the wind field derived from a weather prediction model to retrieve two-dimensional delay distribution, and applied it to Envisat/ASAR interferograms around the California. Li et al. [15] used the precipitable water vapor (PWV) data derived from the MERIS multi-spectrum observation. The unique advantage of using the MERIS data is that the MERIS is equipped with the Envisat satellite, enabling us to observe infrared images simultaneously with SAR images. Recently. Yu et al. [16] developed the global delay model calculation service named the Generic Atmospheric Correction Online Service for InSAR (GACOS) that uses the High-resolution ECMWF weather model (HRES) data. The GACOS model estimates the ZTD by the iterative tropospheric decomposition model to enhance the reproducibility of the actual tropospheric delay. Advantages using numerical weather simulation outputs for InSAR neutral atmospheric delay correction stem from that numerical weather simulations can be available at anytime everywhere. Although spatial resolution of numerical weather simulations ranges from hundred meters to tens of kilometers at now which is insufficient to resolve smaller scale water vapor fluctuation seen in InSAR images, significant reproducibility of long-wavelength (tens of kilometers or longer) delays has been validated in previous researches [12], [13]. On the other hand, external sources also have some advantages compared to numerical weather simulations. For example, the use of GNSS atmospheric observations can observe integrated water vapor with high sampling interval (from seconds to hours) and accuracy as high as radiosonde observations [17]. In addition, the GNSS observation reflects the actual state of the atmosphere as well as InSAR observations. These characteristics of GNSS observation seems hopeful for InSAR neutral atmospheric delay correction.

Recently, Arief and Heki [18] proposed a novel idea that used not only the wet component of the GNSS ZTD (zenith wet delay, ZWD) but also the horizontal gradient of the propagation delay to retrieve the two-dimensional water vapor distribution with the spatial scale of tens of kilometers. In this model, they used the fact that the delay gradient is not sensitive to the observation height in contrast to the ZTD. Using all the data of Japanese GNSS network GEONET for the gradient and only the low altitude stations for the ZWD, they successfully retrieved the water vapor distribution in the case of the typhoon landing on July 2018, even when the interior region of the typhoon located far from the coastline. Although their model only showed the retrieval ability for the spatial scale of a few tens of kilometers, the idea to use the GNSS gradient seems effective to improve the spatial resolution of the delay distribution retrieved by the GNSS.

The purpose of this study is to develop a new model for mitigating InSAR neutral atmospheric delay by use of GNSS atmospheric observations including the delay gradient as well as the ZTD. My proposed model was developed by modifying the method shown in Arief and Heki [18], where the difference is that 1) the proposed model uses all GNSS ZTD data, instead of ZWD data only near the coast, 2) the proposed model estimated the linear delay-altitude dependence in addition to the gridded ZTD field, and 3) the horizontal grid spacing was finer in the proposed model (5 km) than that of Arief and Heki's model (approximately 20 km). The proposed model was validated by applying it to actual interferograms, and then compared with other InSAR delay correction models to evaluate the effectiveness of the proposed model. In the following sections the section 2 describes the brief theory of the proposed model and data used in this study, and the research setting for the model validation is written in the section 3. The section 4 shows modeling results of the proposed delay model and its application to actual interferograms. This section also shows the comparison result of the proposed model with other correction model. Sections 5 and 6 describe the discussion and the summary of this study.

II. Data and Methods

A. Principle of the propagation delay effect in the neutral atmosphere

In space geodetic techniques using the microwave such as the GNSS, InSAR and the Very Long Baseline Interferometry (VLBI), the observed phase signal contains not only the effect of the surface displacement, but also the atmospheric propagation delay effect which causes the apparent phase change. The propagation delay effect in the neutral atmosphere is caused by the heterogeneous distribution of the atmospheric refractivity, which has larger values compared to that in a vacuum. According to Thayer [19], the refractivity in the neutral atmosphere N can be modeled as,

$$N = 10^6(n-1) = k_1\frac{P_d}{T} + k_2\frac{P_v}{T} + k_3\frac{P_v}{T^2} + N_l \qquad (1)$$

where P_d represents the partial pressure of the dry air in hPa, P_v represents the partial pressure of water vapor in hPa, and T represents the absolute temperature in Kelvin. Because coefficients k_1, k_2, and k_3 should be experimentally determined, in this study I used values of $k_1 = 77.60(K/hPa), K_2 =$

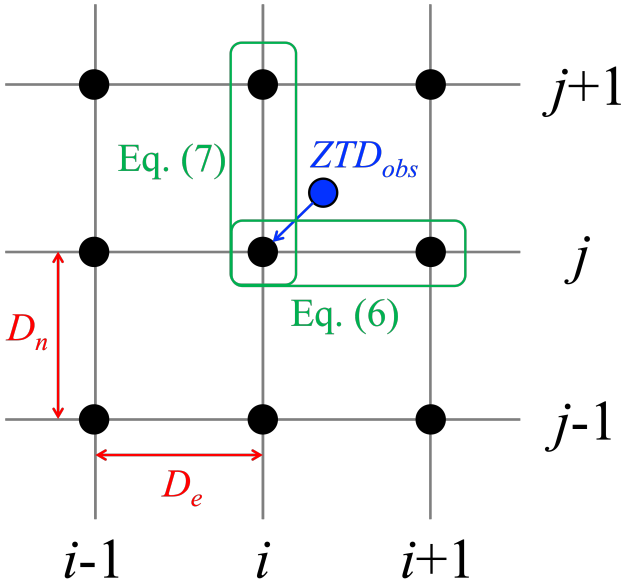

Fig. 1. A conceptual image of the relationship between the model grid and observed ZTD and gradient parameters.

$70.40(K/hPa)$, and $k_3 = 3.739(K^2/hPa)$ derived from Bevis et al. [20].

The amount of the neutral atmospheric delay L_{atm} can be calculated with the line integral of the refractive index n shown in (1) along the microwave path S,

$$L_{atm} = \int_S (n(r) - 1)\, ds + \left(\int_S ds - \int_G ds \right) \tag{2}$$

where r indicates a position from the earth center, G represents the geometrical path between a satellite and a point target on the surface. The first term in the right-hand side represents the change effect of the microwave velocity, and the second term in the right-hand side represents the geometric effect of the path bending that may be evident when the elevation angle is 10° or below.

B. Description of the delay correction model

I proposed a delay correction model for mitigating the InSAR neutral atmospheric delay based on GNSS ZTD and delay gradient observations. As described by MacMillan [21] and Arief and Heki [18], the GNSS slant path delay can be formulated as,

$$SPD = m(\epsilon) \left\{ ZTD + \cdot \cot(\epsilon) \left[G_N \cos(\phi) + G_E \sin(\phi) \right] \right\} \tag{3}$$

where SPD is the total delay along the path direction, ϵ and ϕ represent the elevation angle and the azimuth angle in clockwise from north, respectively. $m(\epsilon)$ is the mapping function that shows the dependence of the delay on the elevation ϵ. G_N and G_E are gradient parameters with north and east directions, respectively. A lot of previous studies introduced that the ZTD can be divided into the hydrostatic contribution (approximately due to dry air) and the water vapor contribution (e.g. [20], [22]). These are called as the zenith hydrostatic delay (ZHD) and the ZWD. Arief and Heki [18] used the ZWD to recover the water vapor and PWV distribution. However, for the InSAR neutral atmospheric delay correction, the ZTD would be appropriate because in principle the propagation delay in InSAR contains both the hydrostatic and wet contribution, although the hydrostatic contribution in InSAR is not so significant due to the relatively small variation in both space and time. Therefore, I used the ZTD instead of the ZWD to construct the delay correction model.

In the model inversion, I at first defined the regularly-gridded sea level ZTD (ZTD_0) with horizontal grid spacing of D_e in the eastern direction and D_n in the northern direction. In addition to the Arief and Heki's formulation, I adopted an additional assumption that the ZTD has a simple linear relationship to the altitude, indicating that the ZTD decreases with increasing the station's height. The model unknown parameters were set as ZTDs at the sea level in each grid and a coefficient representing the height dependence of the ZTD. This can be formulated as,

$$ZTD_{obs} = ZTD_0 + a \cdot h \tag{4}$$

where ZTD_{obs} is the observed ZTD value, a is a coefficient of the height dependence, and h is the GNSS station's altitude.

Following Shoji [23], the observed GNSS delay gradient parameters G_N and G_E can be expressed by using the scale height of ZTD (H_{ZTD}) with a unit of meter, which is the distance where the ZTD decreases by a factor of e (e is the Napier's number), and the horizontal gradient of ZTD (ΔZTD),

$$\boldsymbol{G} = \Delta ZTD \cdot H_{ZTD} \tag{5}$$

where $\boldsymbol{G}$ is the gradient parameter vector with the unit of meters. Using this relationship, the delay gradient can be expressed by ZTD_0 referring Arief and Heki's derivation,

$$G_E = \{ZTD_0(i+1, j) - ZTD_0(i, j)\} \frac{H_{ZTD}}{D_e} \tag{6}$$

$$G_N = \{ZTD_0(i, j+1) - ZTD_0(i, j)\} \frac{H_{ZTD}}{D_n} \tag{7}$$

where i and j represent grid indices in east and north directions, respectively. Here a location (i, j) represents the grid point closest to the GNSS station. I assumed that the observed ZTD closest to the grid location (i, j) is the same as the ZTD at the location (i, j) (Blue dot and vector in Fig. 1). This indicates that I can modify (4) as,

$$ZTD_{obs} = ZTD_0(i, j) + a \cdot h(i, j). \tag{8}$$

(6) and (7) are the case that the GNSS station is located between i and $i+1$ in the eastern direction and j and $j+1$ in the northern direction. The conceptual image of the relationship between the model grid and (6), (7), and (8) is shown in Fig. 1.

The two-dimensional ZTD field was retrieved by the linear least square's inversion. The observation equation can be written in the matrix form as,

$$\boldsymbol{d} = \boldsymbol{A}\boldsymbol{m} \tag{9}$$

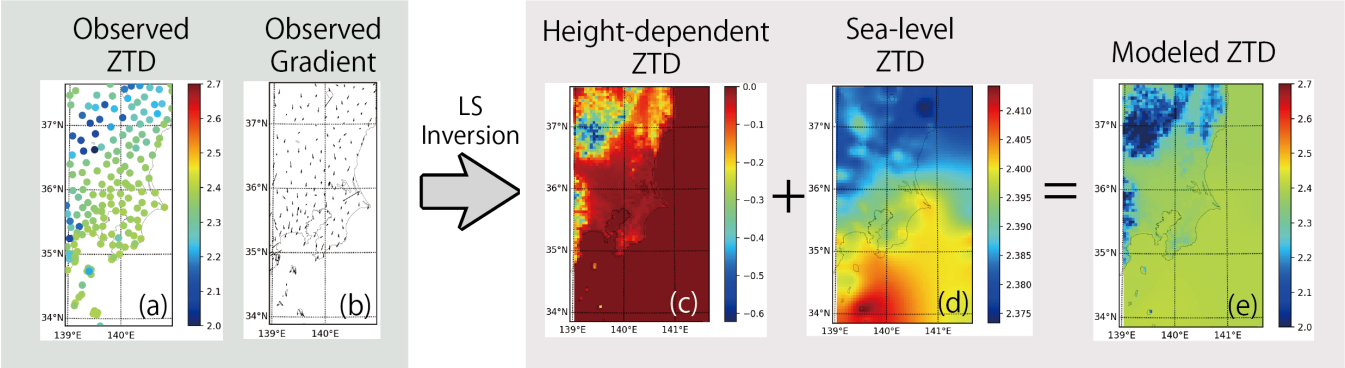

Fig. 2. A brief example of the processing flow in the gridded ZTD retrieval. This example is a case of 02:35 UTC on 23 January 2016. The unit of all color maps is meter.

with

$$\boldsymbol{d} = [ZTD^1_{obs}, \cdots, ZTD^N_{obs}, G^1_E, \cdots, G^N_E, G^1_N, \cdots, G^N_N]^T, \tag{10}$$

$$\boldsymbol{A} = \begin{pmatrix} 0 & 1 & 0 & \cdots & 0 & h^1 \\ \cdots & 0 & 1 & \cdots & 0 & h^2 \\ & & \vdots & & & \\ 0 & \cdots & 1 & \cdots & 0 & h^N \\ 0 & \frac{H_{ZTD}}{D_e} & \cdots & -\frac{H_{ZTD}}{D_e} & \cdots & 0 \\ & & \vdots & & & \\ -\frac{H_{ZTD}}{D_e} & 0 & \cdots & \frac{H_{ZTD}}{D_e} & \cdots & 0 \\ \frac{H_{ZTD}}{D_n} & \cdots & -\frac{H_{ZTD}}{D_n} & 0 & \cdots & 0 \\ & & \vdots & & & \\ 0 & \cdots & \frac{H_{ZTD}}{D_n} & -\frac{H_{ZTD}}{D_n} & \cdots & 0 \end{pmatrix}, \tag{11}$$

and

$$\boldsymbol{m} = [ZTD^1_0, \cdots, ZTD^M_0, a]^T, \tag{12}$$

where $\boldsymbol{d}$ is the data vector of the $3N$ (known) observed values containing N observed ZTDs (ZTD_{obs}), N zonal gradient parameters ($\boldsymbol{G}_E$), and N meridional gradient parameters ($\boldsymbol{G}_N$), all of which are derived from the GNSS processed products. Superscripts shown in (10) is the location identification number of GNSS station, and superscripts in (12) is the consecutive identification number of the model grid point ($M = i \times j$). $\boldsymbol{m}$ is the $M+1$ model parameter vector containing M unknown variables $ZTD_0(i,j)$ and a, and $\boldsymbol{A}$ is the $3N \times (M+1)$ kernel matrix whose component shows the relation between observations and model parameters according to (6), (7), and (8). Here I assumed that the observables follow the normal distribution with the zero-mean and the covariance of Σ. The matrix Σ is set as a diagonal matrix, indicating that the observables have no correlation between each others. In most cases, (9) becomes the under-determined problem due to relatively smaller number of GNSS stations than the number of grid points. To avoid this situation, I added the smoothing constraint by applying the Laplacian operator Δ to ZTD_0 with the free boundary condition, that is,

$$\begin{aligned} \Delta m_{i,j} &= \frac{ZTD_0(i+1,j) - 2ZTD_0(i,j) + ZTD_0(i-1,j)}{D_e^2} \\ &\quad + \frac{ZTD_0(i,j+1) - 2ZTD_0(i,j) + ZTD_0(i,j-1)}{D_n^2} \\ &= 0. \end{aligned} \tag{13}$$

Now the smoothing constraint can be represented in the matrix form as $\boldsymbol{C}$. Therefore, the equation to be solved can be expressed as,

$$\begin{bmatrix} \boldsymbol{d} \\ \boldsymbol{0} \end{bmatrix} = \begin{bmatrix} \boldsymbol{A} \\ \lambda^2 \boldsymbol{C} \end{bmatrix} \boldsymbol{m} \tag{14}$$

where The vector $\boldsymbol{m}$ is estimated by the weighted least squares inversion with the smoothing constraint as,

$$\boldsymbol{m} = \left(\boldsymbol{A}^T \Sigma^{-1} \boldsymbol{A} + \lambda^2 \boldsymbol{C}^T \boldsymbol{C}\right)^{-1} \boldsymbol{A}^T \Sigma^{-1} \boldsymbol{d}. \tag{15}$$

Diagonal elements represent the square of observation error that is derived from the GNSS tropospheric product used in this study. The hyper-parameter λ that controls the relative weight between the observations and the constraint was determined as 0.1 by trial and error to keep both the model resolution and the delay correction effectiveness.

After the inversion, the two-dimensional ZTD field can be constructed by using (4). An example of how the gridded ZTD model is retrieved from the irregularly-located point ZTD data and its gradient data is shown in Fig. 2. To apply this for the InSAR delay correction, the retrieved ZTD field has to be spatially interpolated and then projected onto the InSAR LOS direction. For the interpolation I utilized the bilinear interpolation to the sea-level ZTD (ZTD_0), then the interpolated ZTD_0 was used to calculate the estimated ZTD (ZTD_{model}) at each InSAR pixel. The projection from the zenith direction to the LOS direction to obtain the slant path delay in InSAR (SPD_{InSAR}) was performed by applying the simple trigonometric function with the InSAR incidence angle

(θ) according to the previous studies (e.g. [24]), which can be expressed as,

$$SPD_{InSAR} = \frac{1}{\cos\theta} ZTD_{model}. \tag{16}$$

Finally, estimated delay models with different epochs were subtracted to make the delay difference that can be applicable to the interferogram.

C. InSAR processing

For the InSAR processing, I used the Radar Interferometry Calculation Tools (RINC) version 0.41 [25]. Interferograms were derived from the Phased Array-type L-band Synthetic Aperture Radar 2 (PALSAR-2), an L-band synthetic aperture radar (SAR) sensor on board the Advanced Land Observing Satellite 2 (ALOS-2) launched by the Japan Aerospace Exploration Agency (JAXA) ScanSAR mode data. Because the ALOS-2/PALSAR-2 ScanSAR mode data covers approximately 7 times wider swath (350 km) compared with the ordinary strip-map mode SAR, the use of the ScanSAR data would be more appropriate to assess the effectiveness of the delay correction. To enhance the signal-to-noise ratio and to make the phase unwrapping easier, interferograms were spatially averaged by the multilook processing that reduced the pixel spacing to approximately 90 m in both range and azimuth directions. The orbital and topographic fringes were modeled and removed by using the precise orbit information and the 1 arc-second digital elevation model (DEM) derived from the Shuttle Radar Topography Mission (SRTM). The two-dimensional phase unwrapping was performed by the statistical-cost network-flow algorithm for phase unwrapping (SNAPHU) software version 1.4.2 with the minimum spanning tree (MST) algorithm for the initialization [26]. The long-wavelength phase signal can often be seen in interferograms, which may be caused by the ionospheric/neutral atmospheric delay or the inaccurate orbit information. Although several previous researches (e.g. [27]–[30]) applied the bilinear or quadratic plane fitting correction to reduce it, applying the plane fitting may confuse the evaluation of the delay correction process. Because the orbit information of the ALOS-2 satellite is significantly accurate and such a long-wavelength signal would relates mostly to the propagation delay that I want to mitigate, I did not apply the plane fitting correction for all interferograms.

The obtained initial interferograms theoretically contain both the ionospheric and the neutral atmospheric delay signals. Therefore I at first correct the ionospheric delay signal using the SSM [2] before applying the proposed GNSS-based delay correction. The SSM uses two band-passed single-look complex images, which in common have higher and lower center frequencies f_h and f_l compared with the original center frequency f_c. In this study I split the range frequency band to equally-spaced three parts and used upper and lower parts for the SSM processing. Utilizing the dispersive characteristics in the ionospheric delay effect and the non-dispersive characteristics in the neutral atmospheric delay effect, the SSM estimates the dispersive and non-dispersive components $\Delta\phi_{disp}$ and $\Delta\phi_{non-disp}$ in the interferogram by the linear combination of higher frequency interferogram $\Delta\phi_h$ and lower frequency interferogram $\Delta\phi_l$ as,

$$\begin{aligned}
\Delta\phi_{disp} &= \frac{f_l f_h}{f_c(f_h^2 - f_l^2)}(\Delta\phi_l f_h - \Delta\phi_h f_l) \\
\Delta\phi_{non-disp} &= \frac{f_0}{(f_h^2 - f_l^2)}(\Delta\phi_h f_h - \Delta\phi_l f_l)\,.
\end{aligned} \tag{17}$$

The derived dispersive phase $\Delta\phi_{disp}$ represents the ionospheric delay signal and the remaining non-dispersive phase $\Delta\phi_{non-disp}$ represents the neutral atmospheric delay and others like the surface displacement and unmodeled noises. In practice, the estimated dispersive phase and the non-dispersive phase often show strong small bubble-like noises that may arise from the decorrelation noise or the imperfect unwrapping result in sub-band interferograms. To suppress these undesirable noises, I applied the strong spatial Gaussian filter with the window size of approximately 10 km to the original dispersive phase $\Delta\phi_{disp}$ and then the filtered dispersive phase was subtracted from the original interferogram so that I could obtain the non-dispersive phase, which will be used for the assessment of the proposed GNSS-based delay correction.

D. Propagation delay estimation from other numerical weather models

Later I will show a comparison result of the delay correction effectiveness between the proposed GNSS-based model and delay models based on numerical weather models (NWMs). The atmospheric delay correction using NWMs is now becoming popular for InSAR surface deformation researches (e.g. [31]–[35]). The most representative one contributing to the prevalence of the InSAR delay correction is the publication of the online delay model calculation tool named GACOS [16]. In this study I used two NWM-based delay correction models; the GACOS and the delay model based on the MesoScale Model (MSM) in Japan Meteorological Agency (JMA) for the comparison with my proposed correction method.

The GACOS model is an online delay model calculation service based on the 6 hourly ECMWF-HRES data. The spatial resolution of the HRES model is approximately 10 km with 137 vertical layers from the surface to 0.1 hPa, indicating that the GACOS model cannot resolve meteorological phenomena with spatial scales of a few kilometers or less. On the other hand, the MSM model is a kilometer-scale regional weather forecast model in Japan. I use objective analysis data (initial input data) for the MSM model, which provides every three hours with the horizontal grid spacing of 5 km at the surface and 10 km at all pressure levels. Kinoshita et al. [6] showed that the delay correction using MSM data for ALOS/PALSAR interferograms resulted in statistically comparable performance with that using the WRF simulation. There has not been any studies that compared statistically the correction effectiveness between the GACOS and the MSM objective analysis data.

The delay amount for the MSM-based delay model was calculated using (1) and (2) based on the method shown in [24], whose method assumes that the bending effect in (2) can be negligible due to the differentiation nature between

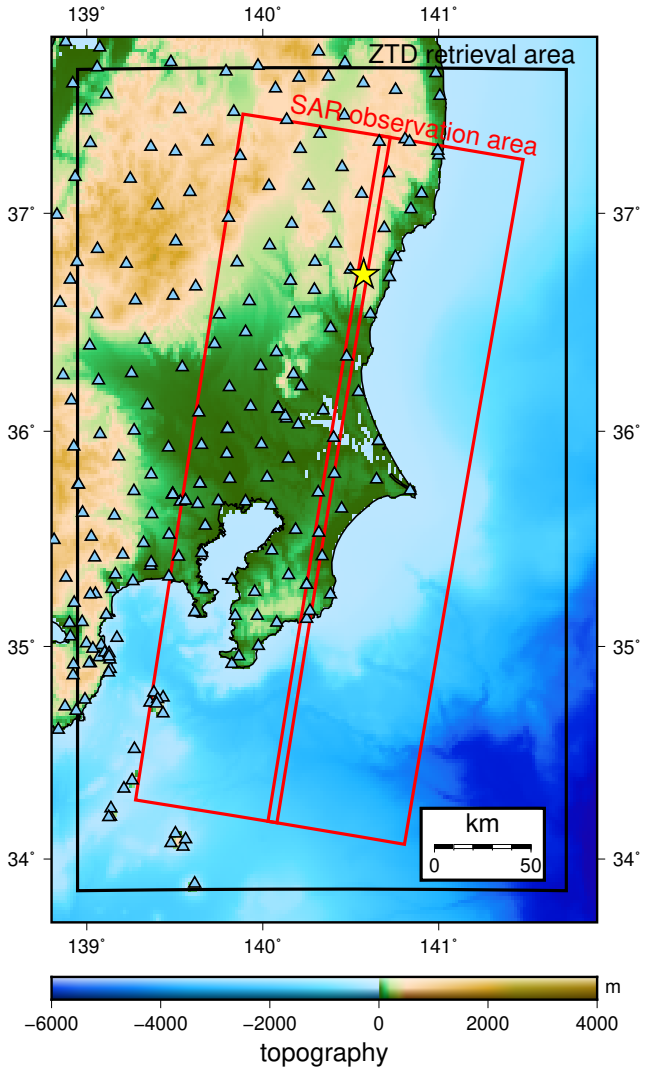

Fig. 3. Geographic condition in this study. The contour color map shows the topography. Black and red rectangles represent the area of the gridded ZTD model and the ALOS-2 SAR coverage, respectively. Triangles colored in light blue represent locations of GNSS stations. The yellow star symbol represents the earthquake epicenter with the Japan Meteorological Agency's magnitude of 6.3 occurred on 28 December 2016.

two epochs in InSAR processing. For computational efficiency, I assumed that the slant path delay can be approximated as the projection of the zenith path delay with the simple trigonometric function. (2) is then modified as,

$$L_{atm} = \frac{1}{\cos\theta}\int_{z_{surface}}^{z_{top}} (n(r) - 1)\, dz \tag{18}$$

where θ represents the incidence angle at a pixel, $z_{surface}$ and z_{top} represent altitudes at the surface and the top layer in the NWM (in the case of the MSM objective analysis, z_{top} is approximately 15,000 m), respectively. The integral in the right-hand side of (18) is performed in the zenith direction.

III. Simulation Setting

In this section I describe the simulation setting of the GNSS-based delay model and the InSAR processing.

TABLE I
INTERFEROMETRIC PAIRS PROCESSED IN THIS STUDY.

Reference	Secondary	Time span (days)	Bperp (m)
2016/01/23	2016/03/19	56	77.3
2016/01/23	2016/04/30	98	241.8
2016/01/23	2016/07/23	182	-131.3
2016/01/23	2016/12/24	336	65.9
2016/03/19	2016/04/30	42	164.6
2016/03/19	2016/07/23	126	-208.6
2016/03/19	2016/12/24	280	-11.4
2016/04/30	2016/07/23	84	-373.2
2016/04/30	2016/12/24	238	-175.9
2016/07/23	2016/12/24	154	197.2
2017/04/15	2017/05/13	28	-229.8
2017/04/15	2017/09/30	168	-420.3
2017/04/15	2017/10/14	182	-404.5
2017/04/15	2017/12/23	252	-406.4
2017/04/15	2018/04/14	364	-173.7
2017/05/13	2017/09/30	140	-190.5
2017/05/13	2017/10/14	154	-174.7
2017/05/13	2017/12/23	224	-176.6
2017/05/13	2018/04/14	336	56.0
2017/09/30	2017/10/14	14	15.8
2017/09/30	2017/12/23	84	13.9
2017/09/30	2018/04/14	196	246.5
2017/09/30	2018/09/29	364	-62.2
2017/10/14	2017/12/23	70	-1.9
2017/10/14	2018/04/14	182	230.8
2017/10/14	2018/09/29	350	-78.0
2017/12/23	2018/04/14	112	232.6
2017/12/23	2018/09/29	280	-76.1
2017/12/23	2018/12/22	364	-107.9
2018/04/14	2018/09/29	168	-308.8
2018/04/14	2018/12/22	252	-340.5
2018/09/29	2018/12/22	84	-31.7
2018/09/29	2019/09/28	364	-94.3
2018/12/22	2019/09/28	280	-62.6
2018/12/22	2019/12/21	364	38.7
2019/09/28	2019/12/21	84	101.3
2019/09/28	2020/04/11	196	613.6
2019/12/21	2020/04/11	112	512.2

I chose the simulation area as the Kanto plain in Japan, where there are large numbers of GNSS stations (Fig. 3) and there are large low-altitude areas and some orogenic regions such as Mt. Tsukuba and Hakone area. In this region I can find that the ALOS-2/PALSAR-2 observations with the ScanSAR mode were significantly archived, reaching to 16 SLCs in the path-frame 17-2900 with the WD1 mode. Since the ALOS-2/PALSAR-2 observations span approximately 4 years ranging from January 2016 to April 2020, two kind of surface displacements in the study area have to be cared before applying delay corrections. The one is an earthquake occurred on 28 December 2016 at northern Ibaraki prefecture with the JMA magnitude of 6.3 (the yellow star symbol in Fig. 3) [28], and another one is the secular subsidence in the north-eastern Chiba prefecture with a maximum subsidence velocity of approximately 2 cm/year (Press release from Chiba prefecture 2020, written in Japanese). Therefore, I used only interferograms that do not include the earthquake signal and that the time span of SLC pairs do not exceed 1 year. Information about the processed interferograms including observation dates, time span, and perpendicular baselines is shown in Table 1.

For the GNSS delay model, the model grid spacing was

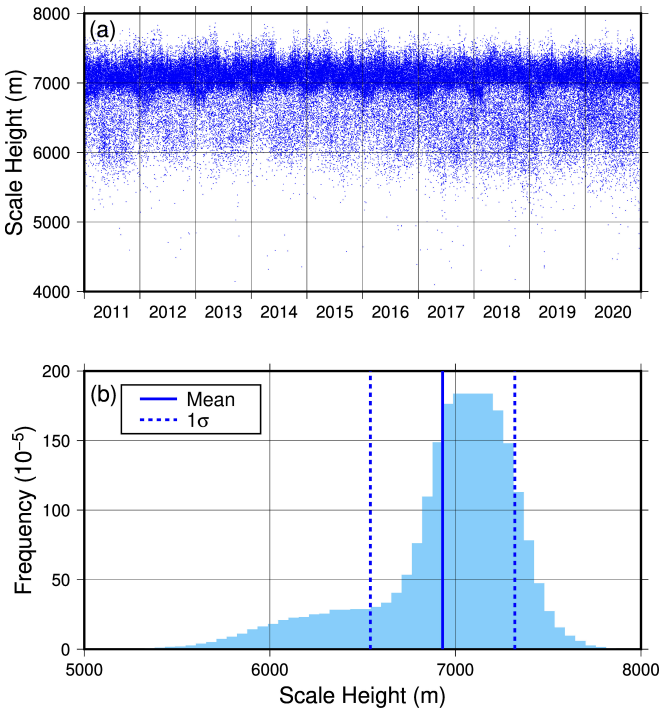

Fig. 4. (a) The ZTD scale height time series estimated from the radiosonde observation located in Japan. (b) The frequency distribution of estimated ZTD scale heights. The vertical solid line represents the mean value and two vertical dashed lines represent the range of 1σ from the mean value.

set as 5 km by considering the model reproducibility and the computational efficiency. The scale height of the ZTD was estimated in this study using radiosonde data in Japan, which will be shown in the latter section. The hyper-parameter of the smoothing constraint in the inversion was set as 0.01 that was determined by trial and error. The gridded ZTD model area fully covers the observation area of interferograms (Fig. 3). As for the GNSS observation data, I used the Precise Point Positioning (PPP) solution every 5 minutes processed and provided by the Nevada Geodetic Laboratory at University of Nevada [36].

IV. Results

A. ZTD scale height estimation

Before conducting the GNSS ZTD distribution retrieval, I investigated the scale height of the ZTD by use of decadal radiosonde observations in Japan. The operational radiosonde observation is performed every half a day on 00 UTC and 12 UTC (9 and 21 JST in local time) in Japan. I used all the available radiosonde data located within Japan (16 stations) for 10 years ranging from 2011 to 2020. I at first calculated ZTD profiles from radiosonde observation data and then fitted the simple exponential curve to estimate the height where the ZTD value decreases by a factor of $1/e$, which is the definition of the scale height.

Fig. 4a showed the time series of estimated ZTD scale heights. The time series clearly showed that there was a moderate annual fluctuation and a large random variation but I could not find any long-term secular trends in ZTD scale heights in each observation. Fig. 4b showed a probabilistic distribution of ZTD scale heights derived from the radiosonde observation. Although the histogram of the estimated ZTD scale height in Fig. 4b indicated that the distribution was skewed to the higher value from the normal distribution, I do not further investigate the cause of this skewness. The mean value of ZTD scale height estimates was calculated as 6930.8 m with the standard deviation of 389.2 m. Hereafter the rounded value of 7000 m was used as the ZTD scale height value for our proposed GNSS ZTD model.

B. InSAR ionospheric correction results

The result of applying the ionospheric delay correction to L-band interferograms showed a significant phase noise reduction. Fig. 5a and 5b is a sample visual image of an interferogram before and after the ionospheric delay correction. The long-wavelength phase variation appeared in the original interferogram (Fig. 5a) was effectively removed by the SSM ionospheric delay correction, although there were residual long- and short-wavelength phase variations in the ionosphere-corrected interferogram (Fig. 5b), most of which would be the delay due to the neutral atmosphere. The ionospheric delay correction was applied to all the interferograms listed in Table 1, whose results were summarized as a scatter plot of the whole scene phase standard deviation before and after applying the ionospheric delay correction (Fig. 6). Fig. 6 indicates that phase variations in original interferograms were significantly decreased for 32 out of 36 interferograms except for 2 interferograms that those phase standard deviations were increased by the ionospheric correction, indicating the SSM was not worked appreciably for these two interferograms. The average reduction of the phase standard deviation for all interferograms by the ionospheric delay correction was 65.96 % (from 102.87 mm to 35.02 mm). In the following, ionosphere-corrected interferograms are used as those for targets of the proposed neutral atmospheric delay correction.

C. Retrieving gridded ZTD by GNSS

The retrieval of the gridded ZTD distribution based on the observed point ZTD data and the ZTD gradient showed significant reproducibility. Fig. 2 shows a retrieval example at 02:35 UTC on 23 January 2016. In Fig. 2, the retrieved gridded ZTD Fig. 2e) showed significant reproducibility by comparison with the observed ZTDs (Fig. 2a). The bias and standard deviation of the ZTD residual between modeled and observed ZTDs at 02:35 UTC on 23 January 2016 was 0.091 mm and 2.03 mm, respectively. I calculated the average bias and standard deviation of the ZTD residual in all ALOS-2 observation days (16 days) that was 0.14 mm and 2.89 mm, respectively. The statistics of ZTD residuals was shown in Table 2, which also indicates that the proposed ZTD retrieval algorithm worked well.

To clarify the improvement of adding the linear height dependence term in (4), I calculated the gridded ZTD without the height dependence term. The result showed that the average RMSE between retrieved and observed ZTDs worsened in the case of no-height dependence (25.65 mm) compared to

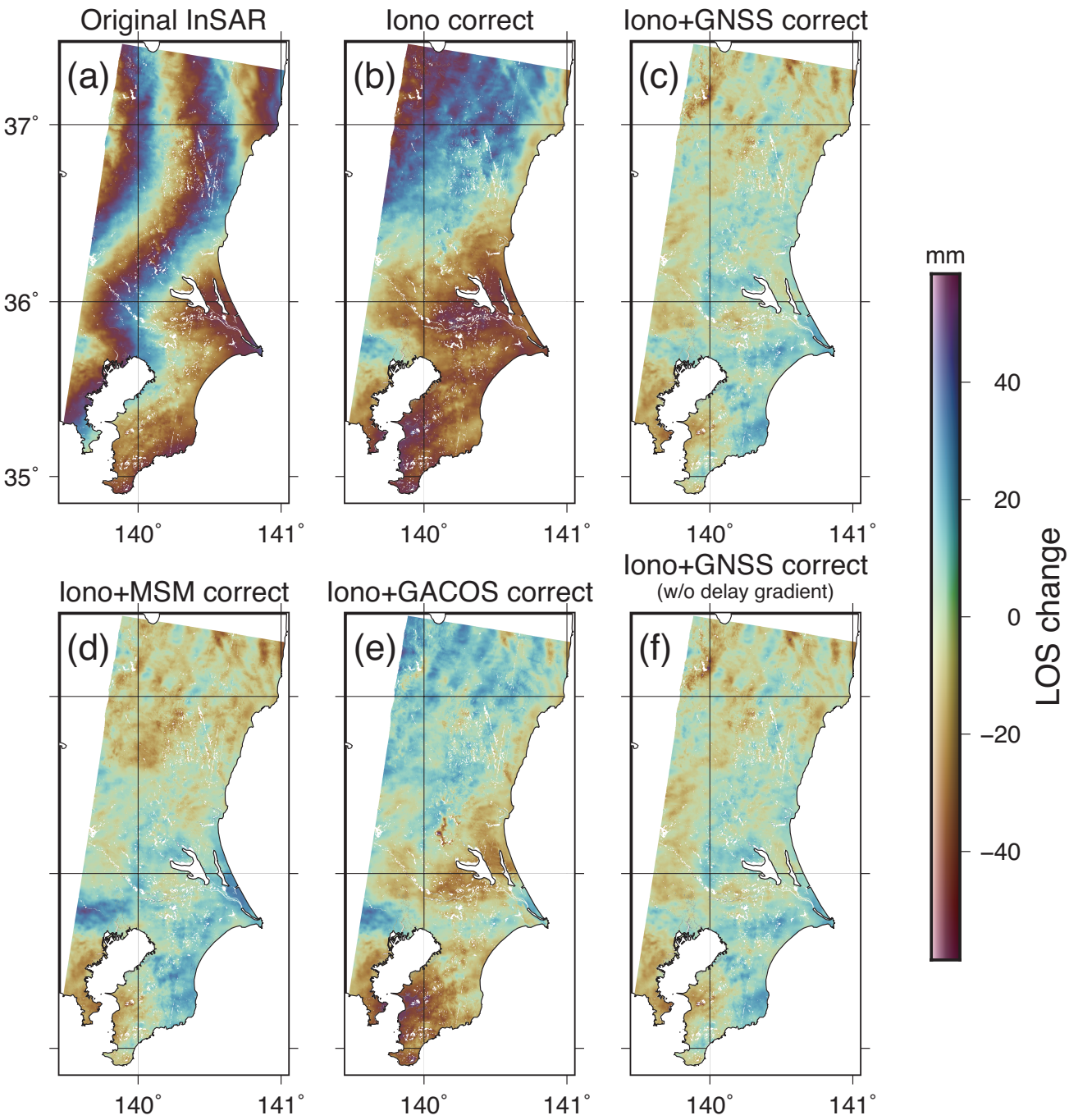

Fig. 5. (a) An original wrapped interferogram of 19 March 2016 and 30 April 2016 over Kanto region. No corrections were applied in this image. (b) An interferogram that the ionospheric correction was applied to the interferogram (a). (c-e) Phase residuals corrected for the GNSS-based , MSM, and GACOS delay model, respectively. (f) A phase residual that corrected by the GNSS-based delay model without the delay gradient. The model phase was subtracted from (b).

that with the height dependence (2.89 mm shown in Table 2). Therefore, I conclude that adding the linear height dependence in (4) significantly contributes to improve the ZTD reproducibility.

D. Result of applying GNSS-based delay correction to interferograms

By applying the proposed GNSS-based delay correction model described in the section 2 to ionosphere-corrected interferograms, I assessed the reproducibility of the new delay correction model in the real interferogram. I applied the proposed delay correction model to in total 36 interferograms derived from the 16 ALOS-2 ScanSAR SLCs. Fig. 5 is an example that shows interferograms before and after the ionospheric and neutral atmospheric delay corrections. All the images in Fig. 5 is derived from the InSAR pair of 19 March 2016 and 30 April 2016 with the perpendicular baseline of 164.6 m. Comparing the interferogram with the ionospheric and neutral

TABLE II
STATISTICS OF THE GRIDDED ZTD RETRIEVAL RESULT.

Date	Model with height dependence		Model without height dependence	
	mean of residual (mm)	STD of residual (mm)	mean of residual (mm)	STD of residual (mm)
2016/01/23	0.09	2.03	0.08	25.24
2016/03/19	0.06	2.98	-0.20	28.07
2016/04/30	0.12	2.52	-0.15	26.31
2016/07/23	0.18	2.79	-0.33	28.98
2016/12/24	0.08	2.48	-0.25	25.20
2017/04/15	0.15	3.78	-0.25	26.70
2017/05/13	0.12	2.79	-0.51	28.27
2017/09/30	0.15	3.39	-0.27	25.85
2017/10/14	0.14	3.18	-0.21	26.61
2017/12/23	0.10	2.45	-0.30	23.11
2018/04/14	0.12	2.73	-0.22	25.46
2018/09/29	0.18	3.26	-0.62	26.44
2018/12/22	0.23	3.45	-0.17	24.16
2019/09/28	0.22	3.37	-0.16	25.73
2019/12/21	0.14	2.72	-0.43	22.26
2020/04/11	0.10	2.40	-0.40	22.18
Average	0.14	2.89	-0.28	25.65

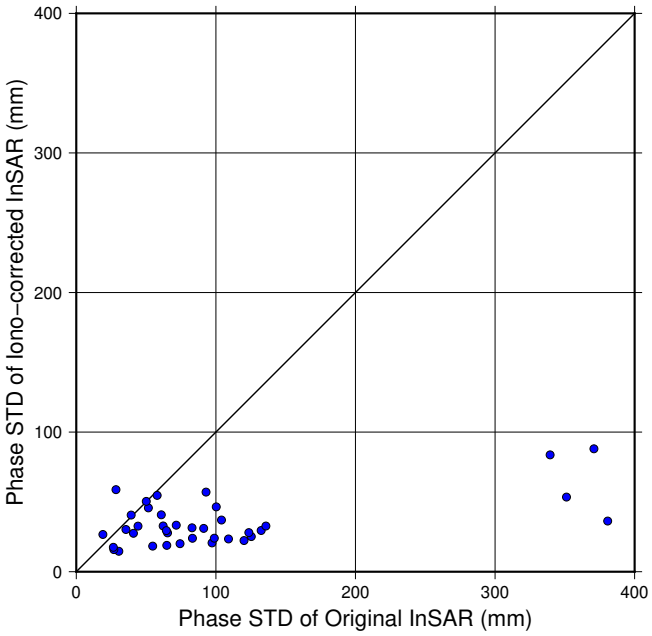

Fig. 6. Phase standard deviation differences from original interferograms against ionosphere-corrected interferograms. Each dot represents the single interferogram.

atmospheric delay correction (Fig. 5c) to that with only the ionospheric delay correction (Fig. 5b), it is visually clear that the residual long-wavelength phase variation shown in Fig. 5b was effectively modeled and removed in Fig. 5c. This indicates that the proposed GNSS-based delay correction model has an ability to model the large spatial scale (an order of tens of kilometers or larger) phase delay signal. However, it is also noted that the corrected interferogram (Fig. 5c) contains residual smaller scale (an order of few tens of kilometers or less) phase variations, most of which would be turbulent delay components associated with atmospheric turbulences and convections. Residual small scale delays in Fig. 5c have an amplitude of approximately $\pm$ 20 mm with the phase standard deviation in the whole scene of 10.43 mm. Because the whole scene phase standard deviation in the interferogram before applying the GNSS-based delay correction (Fig. 5b) was 33.35 mm, the proposed GNSS-based delay correction model significantly reduced the phase standard deviation by 68.72 % in this case. I summarized the difference of the whole scene phase standard deviation before and after applying the GNSS-based delay correction for all pairs as blue circles in Fig. 7. As a whole, most of the pairs showed the decrease of the phase standard deviation by applying the GNSS-based delay correction, although 2 interferograms showed a slight increase and other 2 pairs showed no change. The average reduction of the whole scene phase standard deviation became 33.87 % (from 35.02 mm to 23.16 mm).

Other atmospheric delay corrections using the GACOS and MSM both showed statistically positive impacts (both correction models reduced the whole scene phase standard deviation for large number of interferometric pairs). An example of the corrected interferograms are shown in Fig. 5d and 5e. The GACOS-corrected interferogram (Fig. 5e) could significantly reduce the topography-correlated stratified delay but I could see there remained long-wavelength delays that extended in the north-south direction and was not correlated to the topography (probably it is the turbulent component). On the other hand, the MSM-corrected interferogram in Fig. 5d also effectively reduced the stratified delay. Moreover, the MSM correction could mitigate part of long-wavelength turbulent delay components that was remained in the GACOS-corrected interferogram (Fig. 5e). Considering the fact that the MSM model is a regional mesoscale weather model developed for weather forecasting around Japan and has finer horizontal grid spacing than the ECMWF-HRES model used in the GACOS model, I suggest that the MSM-based InSAR delay correction has a better reproducibility than the GACOS correction in the case of Japan. Whole scene phase standard deviations of the GACOS- and MSM-corrected interferograms in the case of the interferometric pair of 19 March 2016 and 30 April 2016 became 15.97 mm and 12.62 mm, respectively.

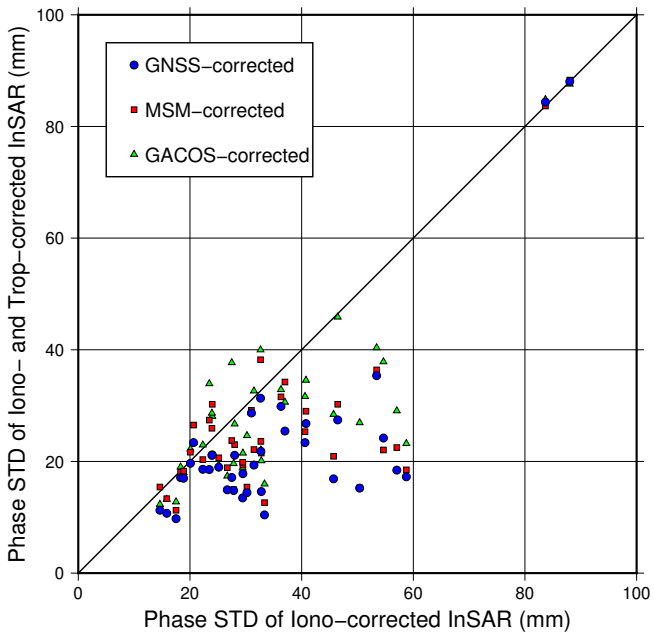

Fig. 7. Phase standard deviation differences from ionosphere-corrected interferograms (shown in Figure 6) against interferograms corrected by the SSM and neutral atmospheric delay models. Each dot represents the single interferogram. Blue circles, red rectangles, and green triangles represent interferogram phase standard deviations corrected by the GNSS-based delay model, the MSM, and the GACOS, respectively.

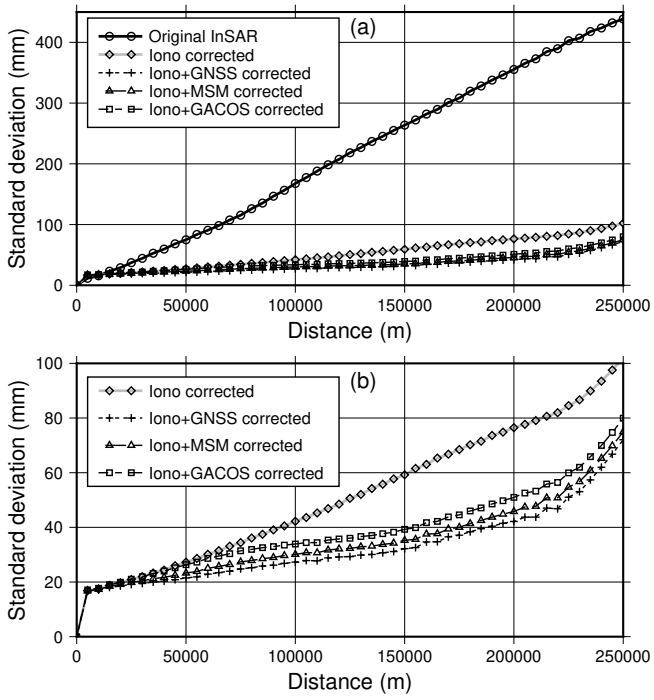

Fig. 8. (a) A figure representing phase standard deviations as a function of distance. Circles with a solid bold black line is derived from interferograms without any corrections, diamonds with dashed black line is from ionosphere-corrected interferograms, plus symbols, triangles, rectangles with dashed lines are from interferograms with the GNSS-based correction, the MSM correction, and the GACOS correction, respectively. (b) Enlarged view of (a) to focus the difference between three neutral atmospheric delay correction models. The original interferogram is omitted in (b).

As can be seen in Fig. 5, the GNSS-based correction (Fig. 5c) outperformed other correction models in the case of the interferometric pair of 19 March 2016 and 30 April 2016. This conclusion can be seen in the overall cases. I summarized the whole scene phase standard deviation of each pair with the proposed GNSS-based delay correction, the GACOS correction, and the MSM correction in Fig. 7. Fig. 7 shows the scatter plot of whole-scene phase standard deviations before and after delay corrections. If the delay correction worked and the phase standard deviation was decreased, the scatter locates below the equivalent line represented as the bold black line in Fig. 7. Fig. 7 clearly shows that in most of interferometric pairs the largest reduction of the phase standard deviation was done by the GNSS-based delay correction (blue circles in Fig. 7). On the other hand, the GACOS correction (green triangles in Fig. 7) showed the worst performance among three correction methods. The MSM correction showed the intermediate performance between the GNSS-based correction and the GACOS correction. All pairs' average of the whole scene phase standard deviation after applying the GACOS correction and the MSM correction became 29.31 mm (16.31 % reduction) and 26.04 mm (25.64 % reduction), respectively.

Finally, I evaluated the relationship between the geometrical distance and the phase standard deviation by use of the semi-variogram like plot [6], which is shown in Fig. 8. As can be seen from Fig. 8, the ionospheric correction and the neutral atmospheric correction both reduced the phase standard deviation in any distances. Focusing on the difference between three neutral atmospheric delay corrections, the GNSS-based correction showed the most reduction in all distances. On the other hand, the GACOS correction showed the worst performance among the three correction models, which is consistent with the result of the phase standard deviation analysis. Fig. 8 clearly indicated that, although relationships between the phase standard deviation and the distance have the monotonically increasing characteristics, all three neutral atmospheric corrections efficiently reduced the phase standard deviation especially in longer distance (over 100 km). In relatively shorter distance (100 km or less), reproducibilities of the neutral atmospheric delay in three corrections were relatively low, suggesting that kilometer-scale turbulent components of the neutral atmospheric delay is still difficult to be precisely modeled. This characteristics was in particular evident in the GACOS correction (rectangles in Fig. 8b, the line approached asymptotically to the line of the ionosphere-corrected interferograms) due to a relatively lower spatial resolution of the ECMWF-HRES model used in GACOS.

E. Sensitivity test of excluding ZTD gradient information

In this subsection, I investigate the model sensitivity in terms of the use of ZTD gradient information, which is one of key idea in this study. To clarify this, I calculated average values of all scene phase standard deviation in cases with and without gradient information. The experiment here also investigates the sensitivity of the correction ability in terms of the spatial density of available GNSS stations by numerically thinning out the input GNSS stations. Fig. 9

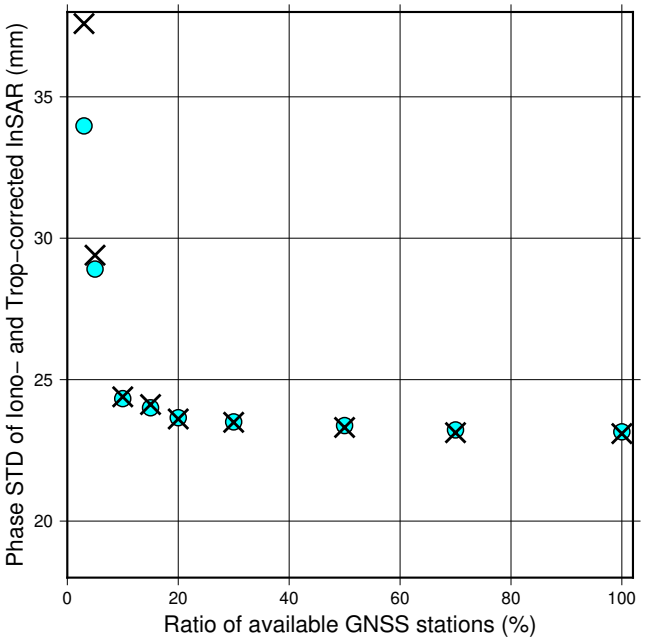

Fig. 9. A scatter plot that represents average values of all scene phase standard deviations as a function of the number of available GNSS stations. Cyan dots represent phase standard deviations after applying the delay correction with ZTD gradient data, and black crosses represent that without gradient data.

represents the summary of this experiment. Fig. 9 indicated that the delay correction without gradient data (black crosses in Fig. 9) indicated a comparable performance as a whole but slightly outperformed that with gradient data (cyan dots in Fig. 9) in the case of high GNSS station ' s density (for example, a case that the ratio of available GNSS stations is 70 % of the total number of stations). As a specific example, Fig. 5(f) shows a corrected interferogram by the GNSS-based delay model without the delay gradient with the ratio of 100 %. As can be seen from Fig. 5(c) and (f), there were no visually significant differences between them. However, the correction with gradient data outperformed that without gradient data in the case of fewer available GNSS stations (lower GNSS density). Therefore, the use of the ZTD gradient information improves the delay correction ability under lesser GNSS stations.

V. Discussion

In my test case, the proposed GNSS-based delay correction model outperformed other two correction models (the MSM and the GACOS) in terms of the phase standard deviation in the whole scene (Fig. 7) and the relationship between the phase standard deviation and the distance (Fig. 8). This study finally evaluated the phase standard deviation with the neutral atmospheric delay correction as 23.16 mm. This value is, as a matter of fact, relatively worse compared to previously derived values. For instance, Yu et al. [16] evaluated the correction performance of the GACOS model (ECMWF-HRES and GNSS ZTD data with the iterative tropospheric decomposition method) by applying it to Sentinel-1 interferograms at eight globally-chosen areas and concluded that the phase standard deviation of the corrected interferograms became approximately 10 mm. Xiao et al. [37] also evaluated the performance of the GACOS model in Eastern China for more than 1000 Sentinel-1 interferograms, resulting in on average 36.4 % reduction (from 3.82 rad to 1.95 rad, which is equivalent to 1.69 cm and 0.86 cm) of the phase standard deviation. Shen et al. [38] developed a ECMWF-HRES based correction model whose magnitude is scaled in a spatially varying manner. Their model was applied to 53 small baseline Sentinel-1 interferograms at the Altyn Tagh Fault and the phase root mean square error relative to the GNSS decreased up to 60 % by applying this model. Bekaert et al. [39] compared several correction methods and concluded that the correction method using the spectrometer (the Medium Resolution Imaging Spectrometer and the Moderate Resolution Imaging Spectroradiometer) showed the largest reduction of the phase root mean square, which became 1-2 cm by the delay correction. Although these previous studies showed better phase standard deviations than the value in this paper, it should be noted that all of them used the Sentinel-1, whose radar wavelength is C-band, and most of cover areas had different climatic conditions compared to this study. Japan is one of regions with largest weather variations and with abundant atmospheric water vapor, which causes spatiotemporally highly variable water vapor distribution. The proposed GNSS-based delay correction model thus presented the significant correction ability under the relatively humid region.

One of the deficit of my correction method arises from the fact that its applicability to other regions strongly depends on the number and the spatial density of available GNSS stations in areas of interest. In this study I used the 5-minutes PPP data analyzed and provided by the NGL. The NGL operationally processes various kinds of global and regional operational GNSS network raw data, whose total number of stations reaches more than 19,000 at the time of submission. The problem is the spatially heterogeneous distribution of GNSS stations; most of GNSS stations are installed in developed countries such as European countries, the United States, and Japan, while few stations in large part of tectonically active areas like the India-Himalaya collision zone, the Great Rift Valley in southeast Africa, and the complex tectonics in the Middle East (Fig. 10). On the contrary, the GACOS model uses the global atmospheric prediction model (ECMWF-HRES) and thus it can be available everywhere in the globe. One of solutions to tackle with the poor model spatial coverage is to use other GNSS datasets such as operational local GNSS networks and campaign observation data. By modifying the code of the proposed correction model a little bit, any kind of GNSS atmospheric estimates can be easily utilized in the proposed correction model. Another one of solutions is the fusion of the proposed model and global atmospheric model estimates like the GACOS model, which would be worth a lot being studied in the future.

In this study, some model parameters such as the grid spacing and the smoothing weighting parameter were determined a priori by author's consideration. In terms of the grid spacing, I fixed it as 5 km throughout this study but it may affect

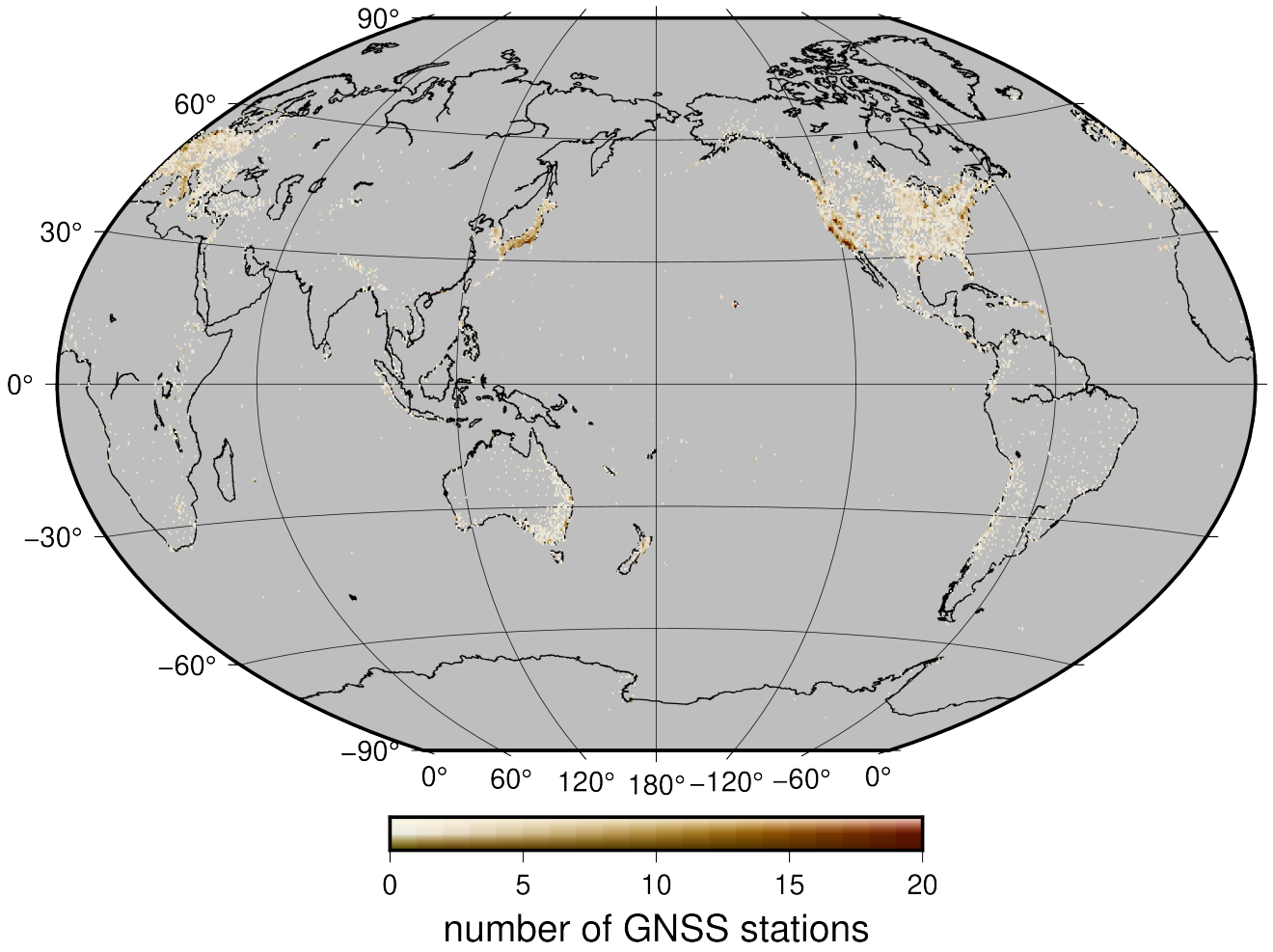

Fig. 10. Global spatial density distribution of GNSS stations processed by the Nevada Geodetic Laboratory (NGL). Colored grids represent the number of GNSS stations in a grid of 0.5° × 0.5°. Grids with the background gray color is where no GNSS stations are available.

the correction accuracy. I investigated the model sensitivity to the grid spacing by changing its value ranging from 3 km to 30 km. As a result, I found that the proposed GNSS delay correction model has little but not negligible sensitivity to the choice of the model grid spacing (Fig. 11). The result of this sensitivity test indicated that the finer the grid spacing was, the better the delay reproducibility became to some extent. Therefore, it would be better to use the finer grid spacing if the significant computer resource can be available, although the difference of the correction ability between coarser and finer grid spacing is not significantly large. The smoothing weighting parameter is another one that should be determined in an objective way. Because this weighting parameter controls the strength of the spatial smoothing, in nature this parameter would be a function of the grid spacing, or in other words, the optimal value of the weighting parameter may become larger with decreasing the grid spacing. In an inversion theory, such a weighting parameter is often determined objectively by the L-curve method (e.g. [40]), the fully Bayesian inversion [41], and the Akaike's Bayesian Information Criteria (ABIC; [42]). The implementation and validation of the objective estimation method for determining the smoothing weighting parameter should be done in a future research.

VI. Conclusion

I developed a new InSAR neutral atmospheric delay correction model based on the GNSS ZTD observations and the horizontal ZTD gradient information. The basic idea of my proposed model was inspired by Arief and Heki's work, and I modified their algorithm by adding the linear height dependence of the ZTD. To determine the scale height of the ZTD that is used in the gridded ZTD retrieval described in the section 2B, I analyzed radiosonde observation data in Japan for 10 years, indicating that the average value of the ZTD scale height was 6930.8 m with the standard deviation of 389.2 m.

The proposed correction model was evaluated using the GEONET, a Japanese operational GNSS observation network, and the ALOS-2/PALSAR-2 ScanSAR interferograms at the Kanto plain in Japan. The interferograms were ionosphere-corrected with the SSM method before applying the proposed neutral atmospheric correction, which decreased the whole scene phase standard deviation by 65.96 % on average (from 102.87 mm to 35.02 mm). The result showed that the proposed model appropriately retrieved observed ZTDs by GNSS; the mean of ZTD residuals became 0.14 mm and its standard deviation as 2.89 mm. The application of the proposed model correction to actual interferograms showed that the proposed

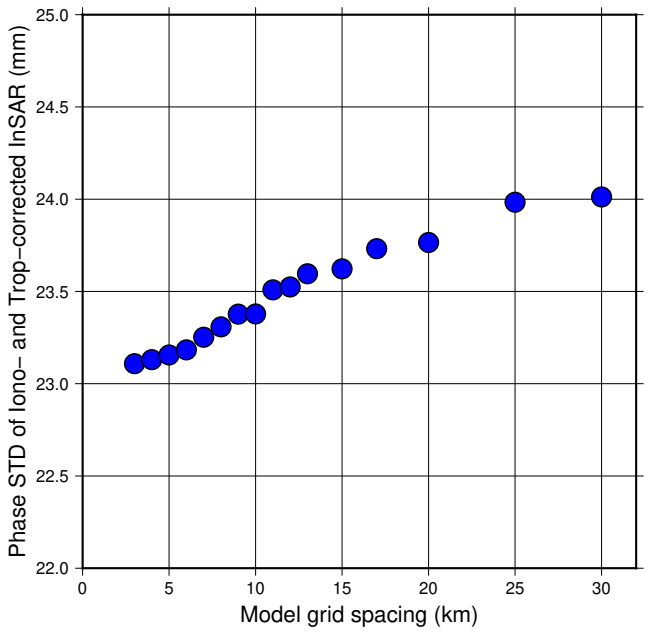

Fig. 11. A scatter plot that represents average values of all scene phase standard deviations as a function of the model grid spacing.

model effectively mitigated the InSAR phase delay, especially that with longer-spatial wavelength (larger than a few tens of kilometers). The phase standard deviation was decreased 33.87 % on average (from 35.02 mm to 23.16 mm).

The correction results were compared with the GACOS model that uses the six-hourly global atmospheric prediction model (ECMWF-HRES) and with the MSM model that is the three-hourly Japanese local mesoscale weather prediction model objective analysis data. By comparison, the proposed correction model exhibited the highest performance in terms of the whole scene phase standard deviation and the distance-phase standard deviation relationship. The sensitivity test indicated that when the number of available GNSS stations in the area of interest is fewer, the use of the delay gradient data for the gridded ZTD retrieval would improve the delay correction ability. On the contrary, the sensitivity test also indicated that the proposed correction model may slightly worsen the delay estimation if there are dense GNSS networks in the area of interest. Although the performance of the proposed GNSS-based correction model depends on the number of available GNSS stations around the InSAR cover area, my result indicated a promising potential of the proposed correction model for a high performance InSAR neutral atmospheric delay correction.

ACKNOWLEDGMENTS

I used the part of the ALOS-2/PALSAR-2 data shared among the PALSAR Interferometry Consortium to Study our Evolving Land Surface (PIXEL). The data were provided by the Japan Aerospace Exploration Agency (JAXA) under a co-operative research contract with the Earthquake Research Institute of the University of Tokyo. The other part of the ALOS-2/PALSAR-2 data was provided by JAXA through the arrangement of JAXA second Research Announcement on the Earth Observations (PI: ER2A2N001). The GEONET GNSS data were originally provided by the Geospatial Authority of Japan, and I used the processed product through the Nevada Geodetic Laboratory, University of Nevada. The MSM data were acquired from the grid point value archive site (http://database.rish.kyoto-u.ac.jp/arch/jmadata/) managed by the Research Institute for Sustainable Humanosphere, Kyoto University. GACOS Atmospheric delay maps can be requested via http://www.gacos.net/. I used the Generic Mapping Toolbox (GMT) and the Matplotlib Python package for drawing all the figures. This study was supported by the Japan Society for the Promotion of Sciences KAKENHI Grant Number 21K14006. The author appreciate three anonymous reviewers for their constructive comments.

REFERENCES

[1] H. A. Zebker, P. A. Rosen, and S. Hensley, "Atmospheric effects in interferometric synthetic aperture radar surface deformation and topographic maps," *J. Geophys. Res.*, vol. 102, no. B4, pp. 7547–7563, 1997.

[2] G. Gomba, A. Parizzi, F. De Zan, M. Eineder, and R. Bamler, "Toward operational compensation of ionospheric effects in SAR interferograms: The split-spectrum method," *IEEE Trans. Geosci. Remote Sens.*, vol. 54, no. 3, pp. 1446–1461, 2015.

[3] B. Zhang, C. Wang, X. Ding, W. Zhu, and S. Wu, "Correction of ionospheric artifacts in SAR data: Application to fault slip inversion of 2009 Southern Sumatra Earthquake," *IEEE Geosci. Remote Sens. Lett.*, vol. 15, no. 9, pp. 1327–1331, 2018.

[4] M. Furuya, T. Suzuki, J. Maeda, and K. Heki, "Midlatitude sporadic-E episodes viewed by L-band split-spectrum InSAR," *Earth Planets Space*, vol. 69, no. 1, pp. 1–10, 2017.

[5] G. Gomba, F. R. González, and F. De Zan, "Ionospheric phase screen compensation for the Sentinel-1 TOPS and ALOS-2 ScanSAR modes," *IEEE Trans. Geosci. Remote Sens.*, vol. 55, no. 1, pp. 223–235, 2016.

[6] Y. Kinoshita, M. Furuya, T. Hobiger, and R. Ichikawa, "Are numerical weather model outputs helpful to reduce tropospheric delay signals in InSAR data?" *J. Geodesy*, vol. 87, no. 3, pp. 267–277, 2013.

[7] Y. Kinoshita and M. Furuya, "Localized delay signals detected by synthetic aperture radar interferometry and their simulation by WRF 4DVAR," *Sci. Online Lett. Atmos.*, vol. 13, pp. 79–84, 2017.

[8] D. T. Sandwell and L. Sichoix, "Topographic phase recovery from stacked ERS interferometry and a low-resolution digital elevation model," *J. Geophys. Res.*, vol. 105, no. B12, pp. 28 211–28 222, 2000.

[9] A. Ferretti, C. Prati, and F. Rocca, "Permanent scatterers in SAR interferometry," *IEEE Trans. Geosci. Remote Sens.*, vol. 39, no. 1, pp. 8–20, 2001.

[10] P. Berardino, G. Fornaro, R. Lanari, and E. Sansosti, "A new algorithm for surface deformation monitoring based on small baseline differential SAR interferograms," *IEEE Trans. Geosci. Remote Sens.*, vol. 40, no. 11, pp. 2375–2383, 2002.

[11] S. Fujiwara, "Baseline determination and correction of atmospheric delay induced by topography of SAR interferometry for precise surface change detection," *J. Geod. Soc. Jpn.*, vol. 45, no. 4, pp. 315–325, 1999, written in Japanese with English abstract.

[12] M.-P. Doin, C. Lasserre, G. Peltzer, O. Cavalié, and C. Doubre, "Corrections of stratified tropospheric delays in SAR interferometry: Validation with global atmospheric models," *J. Appl. Geophys.*, vol. 69, no. 1, pp. 35–50, 2009.

[13] J. Foster, B. Brooks, T. Cherubini, C. Shacat, S. Businger, and C. Werner, "Mitigating atmospheric noise for InSAR using a high resolution weather model," *Geophys. Res. Lett.*, vol. 33, no. 16, 2006.

[14] F. Onn and H. Zebker, "Correction for interferometric synthetic aperture radar atmospheric phase artifacts using time series of zenith wet delay observations from a GPS network," *J. Geophys. Res.*, vol. 111, no. B9, 2006.

[15] Z. Li, E. J. Fielding, P. Cross, and J.-P. Muller, "Interferometric synthetic aperture radar atmospheric correction: medium resolution imaging spectrometer and advanced synthetic aperture radar integration," *Geophys. Res. Lett.*, vol. 33, no. 6, 2006.

[16] C. Yu, Z. Li, N. T. Penna, and P. Crippa, "Generic atmospheric correction model for Interferometric Synthetic Aperture Radar observations," *J. Geophys. Res. Solid Earth*, vol. 123, no. 10, pp. 9202–9222, 2018.

[17] Q. Zhao, Y. Yao, Q. Wang, and Z. Li, "Near-global GPS-derived PWV and its analysis in the El Niño event of 2014–2016," *J. Atmos. Sol.-Terr. Phys.*, vol. 179, pp. 69–80, 2018.

[18] S. Arief and K. Heki, "GNSS meteorology for disastrous rainfalls in 2017–2019 summer in SW Japan: a new approach utilizing atmospheric delay gradients," *Front. Earth Sci.*, vol. 8, 2020.

[19] G. D. Thayer, "An improved equation for the radio refractive index of air," *Radio Sci.*, vol. 9, no. 10, pp. 803–807, 1974.

[20] M. Bevis, S. Businger, S. Chiswell, T. A. Herring, R. A. Anthes, C. Rocken, and R. H. Ware, "GPS meteorology: Mapping zenith wet delays onto precipitable water," *J. Appl. Meteorol.*, vol. 33, no. 3, pp. 379–386, 1994.

[21] D. MacMillan, "Atmospheric gradients from very long baseline interferometry observations," *Geophys. Res. Lett.*, vol. 22, no. 9, pp. 1041–1044, 1995.

[22] J. Davis, T. Herring, I. Shapiro, A. Rogers, and G. Elgered, "Geodesy by radio interferometry: Effects of atmospheric modeling errors on estimates of baseline length," *Radio Sci.*, vol. 20, no. 6, pp. 1593–1607, 1985.

[23] Y. Shoji, "Retrieval of water vapor inhomogeneity using the Japanese nationwide GPS array and its potential for prediction of convective precipitation," *J. Meteorol. Soc. Japan. Ser. II*, vol. 91, no. 1, pp. 43–62, 2013.

[24] R. Jolivet, P. S. Agram, N. Y. Lin, M. Simons, M.-P. Doin, G. Peltzer, and Z. Li, "Improving InSAR geodesy using global atmospheric models," *J. Geophys. Res. Solid Earth*, vol. 119, no. 3, pp. 2324–2341, 2014.

[25] T. Ozawa, E. Fujita, and H. Ueda, "Crustal deformation associated with the 2016 Kumamoto Earthquake and its effect on the magma system of Aso volcano," *Earth Planets Space*, vol. 68, no. 1, pp. 1–15, 2016.

[26] C. W. Chen and H. A. Zebker, "Phase unwrapping for large SAR interferograms: Statistical segmentation and generalized network models," *IEEE Trans. Geosci. Remote Sens.*, vol. 40, no. 8, pp. 1709–1719, 2002.

[27] R. Jolivet, R. Grandin, C. Lasserre, M.-P. Doin, and G. Peltzer, "Systematic InSAR tropospheric phase delay corrections from global meteorological reanalysis data," *Geophys. Res. Lett.*, vol. 38, no. 17, 2011.

[28] Y. Fukushima, S. Toda, S. Miura, D. Ishimura, J. Fukuda, T. Demachi, and K. Tachibana, "Extremely early recurrence of intraplate fault rupture following the Tohoku-Oki earthquake," *Nat. Geosci.*, vol. 11, no. 10, pp. 777–781, 2018.

[29] M. Hashimoto, "Postseismic deformation following the 2016 Kumamoto earthquake detected by ALOS-2/PALSAR-2," *Earth Planets Space*, vol. 72, no. 1, pp. 1–27, 2020.

[30] J. Hu, J. Liu, Z. Li, J. Zhu, L. Wu, Q. Sun, and W. Wu, "Estimating three-dimensional coseismic deformations with the SM-VCE method based on heterogeneous SAR observations: Selection of homogeneous points and analysis of observation combinations," *Remote Sens. Environ.*, vol. 255, 2021.

[31] O. Cavalié and S. Jónsson, "Block-like plate movements in eastern Anatolia observed by InSAR," *Geophys. Res. Lett.*, vol. 41, no. 1, pp. 26–31, 2014.

[32] F. Albino, J. Biggs, C. Yu, and Z. Li, "Automated Methods for Detecting Volcanic Deformation Using Sentinel-1 InSAR Time Series Illustrated by the 2017–2018 Unrest at Agung, Indonesia," *J. Geophys. Res. Solid Earth*, vol. 125, no. 2, 2020.

[33] Y. Himematsu, T. Ozawa, and Y. Aoki, "Coeruptive and posteruptive crustal deformation associated with the 2018 Kusatsu-Shirane phreatic eruption based on PALSAR-2 time series analysis," *Earth Planets Space*, vol. 72, no. 1, pp. 1–12, 2020.

[34] J. Jiang and R. B. Lohman, "Coherence-guided InSAR deformation analysis in the presence of ongoing land surface changes in the Imperial Valley, California," *Remote Sens. Environ.*, vol. 253, 2021.

[35] L. Yongsheng, T. Yunfeng, Y. Chen, S. Zhe, J. Wenliang, L. Zhenhong, Z. Jingfa, L. Yi, and L. Bingquan, "Present-day interseismic deformation characteristics of the Beng Co-Dongqiao conjugate fault system in central Tibet: implications from InSAR observations," *Geophys. J. Int.*, vol. 221, no. 1, pp. 492–503, 2020.

[36] G. Blewitt, W. C. Hammond, and C. Kreemer, "Harnessing the GPS data explosion for interdisciplinary science," *Eos*, vol. 99, 2018.

[37] R. Xiao, C. Yu, Z. Li, and X. He, "Statistical assessment metrics for InSAR atmospheric correction: Applications to generic atmospheric correction online service for InSAR (GACOS) in Eastern China," *Int. J. Appl. Earth Obs. Geoinf.*, vol. 96, 2021.

[38] L. Shen, A. Hooper, and J. Elliott, "A Spatially Varying Scaling Method for InSAR Tropospheric Corrections Using a High-Resolution Weather Model," *J. Geophys. Res. Solid Earth*, vol. 124, 2019.

[39] D. Bekaert, R. Walters, T. Wright, A. Hooper, and D. Parker, "Statistical comparison of InSAR tropospheric correction techniques," *Remote Sens. Environ.*, vol. 170, pp. 40–47, 2015.

[40] P. C. Hansen and D. P. O'leary, "The Use of the L-Curve in the Regularization of Discrete Ill-Posed Problems," *SIAM J. Sci. Comput.*, vol. 14, no. 6, pp. 1487–1503, 1993.

[41] J. Fukuda and K. M. Johnson, "A Fully Bayesian Inversion for Spatial Distribution of Fault Slip with Objective Smoothing," *Bull. Seismol. Soc. Am.*, vol. 98, no. 3, pp. 1128–1146, 2008.

[42] T. Yabuki and M. Matsu'ura, "Geodetic data inversion using a Bayesian information criterion for spatial distribution of fault slip," *Geophys. J. Int.*, vol. 109, pp. 363–375, 1992.

Yohei Kinoshita received the Ph.D. degreein Science from the Hokkaido University, Sapporo, Japan, in 2014. He is currently an assistant professor with the Faculty of the System and Information Engineering, University of Tsukuba, Japan. His research interests include meteorological application of InSAR, atmospheric delay correction for InSAR, measuring surface deformation with space geodetic techniques, and remote sensing for disaster mitigation and urban planning.